Nano Research
2022, 15(7): 5769–5774

ISSN 1998-0124 CN 11-5974/O4
https://doi.org/10.1007/s12274-022-4201-1

Research Article

Direct transformation of ZIF-8 into hollow porous carbons and hollow carbon composites

Lingqi Huang[1,2], Zhiyong Luo[1], Wenjie Han[1], Qi Zhang[1], He Zhu[1] (✉), and Shiping Zhu[1] (✉)

[1] School of Science and Engineering, The Chinese University of Hong Kong, Shenzhen 518172, China
[2] School of Environmental and Natural Resources, Zhejiang University of Science and Technology, Hangzhou 310023, China

Received: 27 November 2021 / **Revised:** 21 January 2022 / **Accepted:** 27 January 2022

ABSTRACT

Hollow porous carbons (HPCs) are a class of porous materials with advantages of high surface to volume ratio, large interior cavities, low density, and short diffusion length, which are promising in various applications. Direct carbonization of carbon precursors is the simplest and the most cost-effective method to prepare porous carbons, however, it often leads to non-hollow structures. Herein, we demonstrate the preparation of HPCs through a direct carbonization method with a two-step heating process of zeolitic imidazolate framework-8 (ZIF-8) and tetrafluoroterephthalonitrile (TFTPN). During the carbonization, ZIF-8 nanoparticles first react with TFTPN at low temperature to create polymer coatings on the surface, which are then converted into HPCs at elevated temperature. The obtained HPCs show hierarchically porous structure with high specific surface areas and pore volumes. Additionally, this method has been adopted to fabricate Au@HPCs yolk–shell composites, exhibiting good catalytic performance in nitrobenzene reduction. The developed synthesis strategy can enrich the toolbox for the preparation of novel HPCs and their composites.

KEYWORDS

porous hollow carbon, carbonization, gold nanoparticles, nitrobenzene reduction

1 Introduction

Porous carbon materials having high thermal and chemical stability, chemical diversity, and high porosity [1, 2] have been extensively used for energy storage [3–5], catalysts [6–8], sensors [9, 10], and adsorbents [11, 12]. Among various carbon forms, hollow porous carbons (HPCs) possess many advantages over traditional non-hollow porous carbons, including high surface to volume ratio, large interior cavities, low density, and short diffusion length. Therefore, the construction of HPCs has received more and more attention.

Metal-organic frameworks (MOFs), as an emerging class of porous materials, have been recently investigated as precursors for the preparation of HPCs, because their superb features such as high porosity, large specific surface area, and controllable pore structure can be inherited by the derived carbons [13, 14]. Generally speaking, it is necessary to create the interior cavities in MOFs before carbonization, thus templates, including hard templates (polystyrene particles, silicas) and soft templates (micelles), are widely used for the synthesis of HPCs. For example, Jiang et al. assembled zeolitic imidazolate framework-8 (ZIF-8) particles onto carboxylic acid modified polystyrene particles, followed by etching the polymer core in a solvent to prepare hollow ZIF-8 spheres. After carbonization, a class of HPCs with high single-atom zinc content and uniform nitrogen active sites could be obtained, exhibiting high efficiency in carbon dioxide conversion [15]. Tan and Zeng reported the growth of ZIF-67 hollow spheres onto vesicles assembled from monomeric species and surfactants. The derived hollow carbon nanocomposites demonstrated excellent oxygen evolution reaction (OER) activities [16]. On the other hand, selective etching has been reported as an alternative to construct hollow MOFs and thus HPCs. For example, Hu et al. synthesized hollow monocrystalline ZIF-8 using tannic acid as the etching agent. The pyrolyzed HPCs showed enhanced Na^+/K^+ ion intercalation performance [17]. Although the use of hollow MOFs as the HPC precursors is a versatile and straightforward strategy, it usually suffers from drawbacks of high cost, complex and cumbersome processes, and limited available combinations.

Direct carbonization of pristine MOF crystals is the simplest and the most cost-effective method, however, it often leads to non-hollow structure. Recently, several works have demonstrated the preparation of HPCs via this method under specific carbonization conditions. Through a thermal treatment of ZIF-67 at 700 °C in Ar/H_2 atmosphere, followed by an acid treatment, N-doped carbon nanotube frameworks with a hollow structure were obtained by Wang and coworkers. The presence of H_2 was critical, without which only common non-hollow porous carbons could be prepared [18]. Mai et al. reported a low-temperature pyrolysis process to prepare HPCs in Ar atmosphere, which exhibited excellent performance in energy conversion and storage [19]. These results are interesting and encouraging, nevertheless, the development of direct carbonization method for the preparation of HPCs is still in its infancy, yet highly desirable.

In our previous work, tetrafluoroterephthalonitrile (TFTPN) was found to be able to react with 2-methylimidazole (2-MeI) to

Address correspondence to He Zhu, zhuhe@cuhk.edu.cn; Shiping Zhu, shipingzhu@cuhk.edu.cn

afford polymeric precursors for the one-step production of porous carbons [20, 21]. Since 2-MeI is the organic ligands in ZIF-8, herein, we further demonstrated the synthesis of HPCs by direct carbonization of ZIF-8 and TFTPN. Upon heating, TFTPN would vaporize, adsorb onto ZIF-8, and react with 2-MeI to produce cross-linked polymers on the surface of ZIF-8, accompanying with the partial decomposition of the frameworks. At elevated temperature, while the carbonization process proceeded, extensive reaction between TFTPN and 2-MeI occurred, leading to the further coordination dislocation and structure collapse, and eventually HPCs were obtained. The proposed protocol was also applicable for the synthesis of Au@HPC nanocomposites, and the obtained materials displayed an efficient catalytic activity in nitrobenzene reduction. This work is expected to offer an alternative convenient and practical method for the synthesis of hollow carbons and carbon hybrids.

2 Results and discussion

ZIF-8 derived HPCs were prepared via a direct carbonization method with a two-step heating process, as shown in Fig. 1 and Fig. S1 in the Electronic Supplementary Material (ESM). ZIF-8 nanoparticles first reacted with TFTPN at 140 °C for 4 h to create polymer coatings on the surface, which were then converted into HPCs at elevated temperature. Carbonizations of ZIF-8 with different amounts of TFTPN were carried out and the corresponding products were denominated as HPC-F_x, where x represents the feed mass ratio of TFTPN to ZIF-8 (Table S1 in the ESM). For comparison, C-F_0 without the use of TFTPN in carbonization was prepared as the control sample.

In Fig. 2(a), the powder X-ray diffraction (PXRD) patterns of all carbons showed amorphous carbon (002) peak at 23.5°–25°. Interestingly, the position of (002) peak shifted from 25° to 23.5° with the increase amounts of TFTPN, suggesting the increased average interlayer distance [17]. The obtained carbon materials all exhibited good thermal stability (Fig. S2 in the ESM). As shown in Fig. 2(b), the X-ray photoelectron spectroscopy (XPS) results confirmed the presence of F, N, and O in all HPC-F_x samples, and N and O in C-F_0. The surface areas and pore structures of all carbons were characterized and calculated from N_2 adsorption–desorption isotherms (Figs. 2(c) and 2(d) and Table S1 in the ESM). At low p/p_0, rapid N_2 uptake was observed due to the presence of abundant micropores. At middle and high relative pressure range of 0.45–0.98, clear hysteresis loops appeared owing to the existence of mesopores. Compared to C-F_0, all HPC-F_x samples showed enhanced hysteresis loops, with HPC-$F_{0.25}$ being the most pronounced, indicating the generation of more cage-type mesopores in the shell [22]. The calculated specific surface areas of HPC-$F_{0.25}$, HPC-F_1, and HPC-F_2 were 585.6, 546.4, and 458.2 $m^2 \cdot g^{-1}$, with pore volumes of 1.25, 1.04, and 0.71 $cm^3 \cdot g^{-1}$, respectively. The decreased surface areas and pore volumes were attributed to the formation of more and denser polymers as the amount of TFTPN increased. In the meantime, the pore size distribution revealed that all HPC-F_x samples contained hierarchical pore structure with main pore size centered at ~ 0.55 and ~ 3.9 nm, however, C-F_0 was mainly microporous. The introduction of mesopores could improve the mass transfer

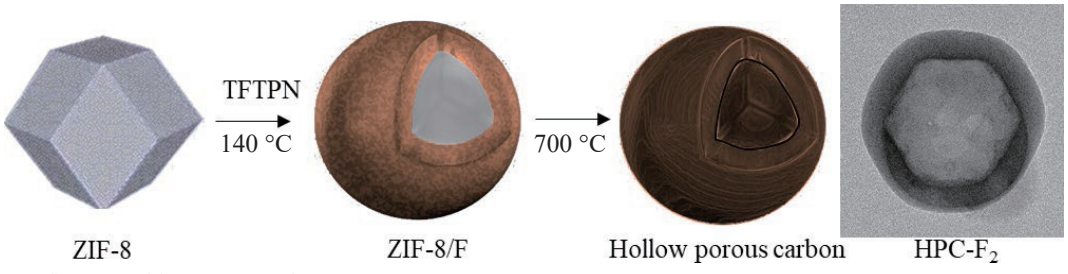

Figure 1 Schematic illustration of the preparation of HPCs.

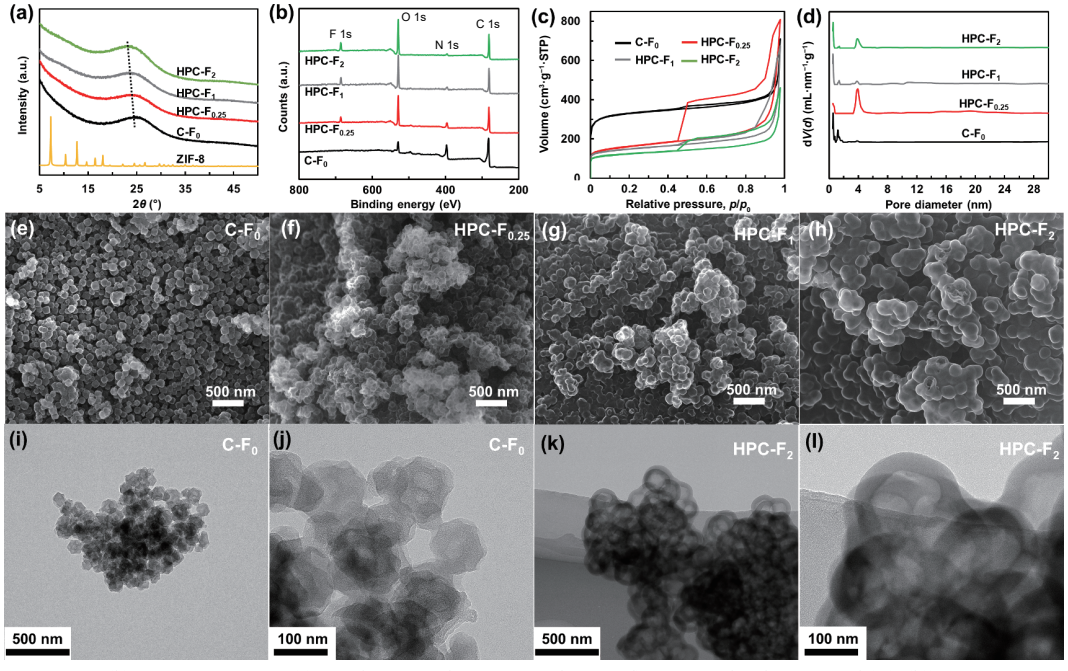

Figure 2 (a) XRD patterns, (b) XPS survey curves, (c) N_2 adsorption–desorption isotherms, (d) pore size distributions, and ((e)–(h)) SEM images and ((i)–(l)) TEM images of ZIF-8 derived carbons.

behavior and thus benefited the application performance of the obtained HPCs.

Next, the morphology was studied by scanning electron microscope (SEM) and transmission electron microscope (TEM). Compared to the polyhedral shapes of C-F_0 (Fig. 2(e)), the HPC-F_x samples exhibited quasi-polyhedral structures (Figs. 2(f)–2(h)). With the increase in the amount of TFTPN (0.25, 1, and 2), the particles became interconnected and more spherical, and their average size increased from 110 ± 23 to 142 ± 31 and then to 181 ± 35 nm. This was owing to the enhanced reaction between TFTPN and ZIF-8, leading to the formation of a thicker polymer shell as well as the interconnection between carbon particles. The broken pieces observed from SEM images (Fig. S3 in the ESM) proved that all HPC samples were hollow in nature, which was then further confirmed by TEM. As shown in Figs. 2(k) and 2(l) and Fig. S4 in the ESM, all samples showed similar particle sizes to those revealed by SEM, and the shell became thicker with the increase in the amount of TFTPN. Additionally, the interior cavities were polyhedral, mimicking the shape of the pristine ZIF-8. However, C-F_0 exhibited solid internal structure, indicating the importance of TFTPN in the formation of interior cavity.

In order to obtain HPCs, the reaction between ZIF-8 and TFTPN to form polymers on the surface of ZIF-8 was the key step and thus was systematically investigated by stopping the heating process after the first step. As shown in Fig. S5(a) in the ESM, the obtained sample appeared brick-red and was named as ZIF-8/F. This color change indicated the formation of new substances on ZIF-8. The SEM images revealed an average diameter of ~ 122 nm and a quasi-polyhedral shape of the polymer coated ZIF-8, similar to those of the pristine ZIF-8 nanoparticles (Fig. S5(b) in the ESM). The ZIF-8/F showed nearly identical diffraction pattern as the pristine ZIF-8 (Fig. S5(c) in the ESM). Importantly, the TEM image suggested that ZIF-8/F was not hollow (Fig. S5(d) in the ESM), indicating that the interior cavity of HPCs was formed in the second step of heating process, where hydrofluoric acid (HF) would possibly generate and etch the core [23, 24]. In Fig. S5(e) in the ESM, thermalgravimetric analysis (TGA) indicated that ZIF-8/F started to degrade at a lower temperature than ZIF-8 and the weight of the final residue was reduced. In Figs. S5(f) and S5(g) in the ESM, the specific surface area decreased significantly from ~ 1,800 $m^2 \cdot g^{-1}$ of ZIF-8 to ~ 377 $m^2 \cdot g^{-1}$ of ZIF-8/F. The pore size distribution analysis revealed that ZIF-8/F showed almost the same microporosity compared to ZIF-8, however, the new appearance of some mesopores in the range of 12–25 nm was observed at the same time. These results all indicated the formation of polymer on ZIF-8.

In order to explore the molecular structure of the polymer, ZIF-8/F was etched in 1 M HCl (excess) to remove the ZIF-8 part. The obtained dark-brown material (named as ZIF-8/F-etched) was characterized with Fourier transform infrared-attenuated total reflection (FTIR-ATR), solid-state nuclear magnetic resonance (ss-NMR), and XPS (Fig. S6 in the ESM). In Fig. S6(a) in the ESM, the ZIF-8/F-etched showed peak bands of HC=CH, methyl group, cyano group, and C–N stretching band at 3,135, 2,924, 2,235, and 1,300 cm^{-1}, respectively, inherited from 2-MeI and TFTPN. The peak at 1,620 cm^{-1} of ZIF-8/F-etched, attributed to the resonance of C=N stretching band, shifted towards higher frequency from 1,595 cm^{-1} of 2-MeI, confirming the formation of phenyl-imidazole bond [25, 26]. In Fig. S6(b) in the ESM, the 13C cross-polarization magic angle spinning (CP-MAS) NMR spectrum of ZIF-8/F-etched showed resonance signals at 9, 106, 118, and 142 ppm, assigning to characteristic of methyl group, cyano group, C–C, and N–C–N, respectively [27]. Additionally, the XPS deconvolution spectra of C 1s and F 1s suggested multiple substitutions of 2-MeI on TFTPN (Figs. S6(c)–S6(f) in the ESM) [28, 29]. Bearing these results in mind, we concluded that in the first step of heating process, TFTPN would vaporize, migrate to, and be captured by ZIF-8 under the nitrogen flow at 140 °C. The adsorbed TFTPN then reacted with 2-MeI via nucleophilic substitution (Fig. S6(g) in the ESM), and since both molecules were multifunctional, cross-linked polymers were formed on the surface of ZIF-8, which would generate HF at elevated temperature and etch the core in the second step of heating process, thus forming the HPCs.

This strategy also allowed us to facile prepare Au@HPC-F_2 nanocomposites. Prior to carbonization, $AuCl_4^-$ ions were loaded into ZIF-8 by direct mixing of salt solution with ZIF-8 aqueous dispersion, followed by filtration and air-drying. It was found that the crystal structures of the resulting composite and ZIF-8 were the same (Fig. S7(a) in the ESM). The surface area slightly decreased from 1,794.3 to 1,643 $m^2 \cdot g^{-1}$, and the total pore volume was marginally reduced from 1.13 to 1.03 $mL \cdot g^{-1}$ (Figs. S7(b) and S7(d) in the ESM), owing to the adsorbed metal ions in the ZIF-8 pores. The composite was then carbonized in the presence of TFTPN to produce Au-hollow porous carbon hybrids. The obtained material was firstly characterized with N_2 adsorption–desorption isotherms, XRD, and TGA. Au@HPC-F_2 showed similar isotherm curves and pore distributions in comparison with HPC-F_2 (Table S1 in the ESM and Fig. 3(a)). In Fig. 3(b), the strong characteristic peaks at ~ 38.4°, ~ 44.5°, and ~ 65° confirmed the formation of gold crystals in Au@HPC-F_2. The weight percentage of gold was estimated to be ~ 6% based on the TGA measurements (Fig. 3(c)).

The morphology and chemical composition were then characterized and presented in Fig. 4 and Fig. S8 in the ESM. The Au@HPC-F_2 showed similar surface morphology to HPC-F_2 as revealed by SEM (Fig. 4(a)). However, Au nanoparticles with a diameter of ~ 29 nm could be clearly observed in the HPCs under TEM Figs. 4(b)–4(d). The elemental mapping images evidently showed that C, N, and O atoms were evenly dispersed on the material, excluding the core region where Au atoms accumulated Figs. 4(e)–4(h). The XPS result of Au 4f spectrum indicated the presence of Au^0 and Au^{3+} (Fig. 4(i)) [30]. The oxidation state was also confirmed with the O 1s spectrum (Fig. 4(j)) [31, 32]. These results demonstrated that the adsorbed $AuCl_4^-$ ions in ZIF-8

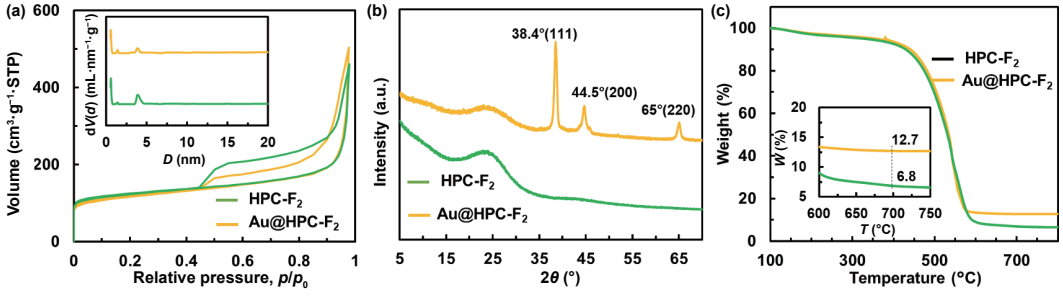

Figure 3 (a) N_2 adsorption–desorption isotherms, and (b) XRD and (c) TGA curves of HPC-F_2 and Au@HPC-F_2.

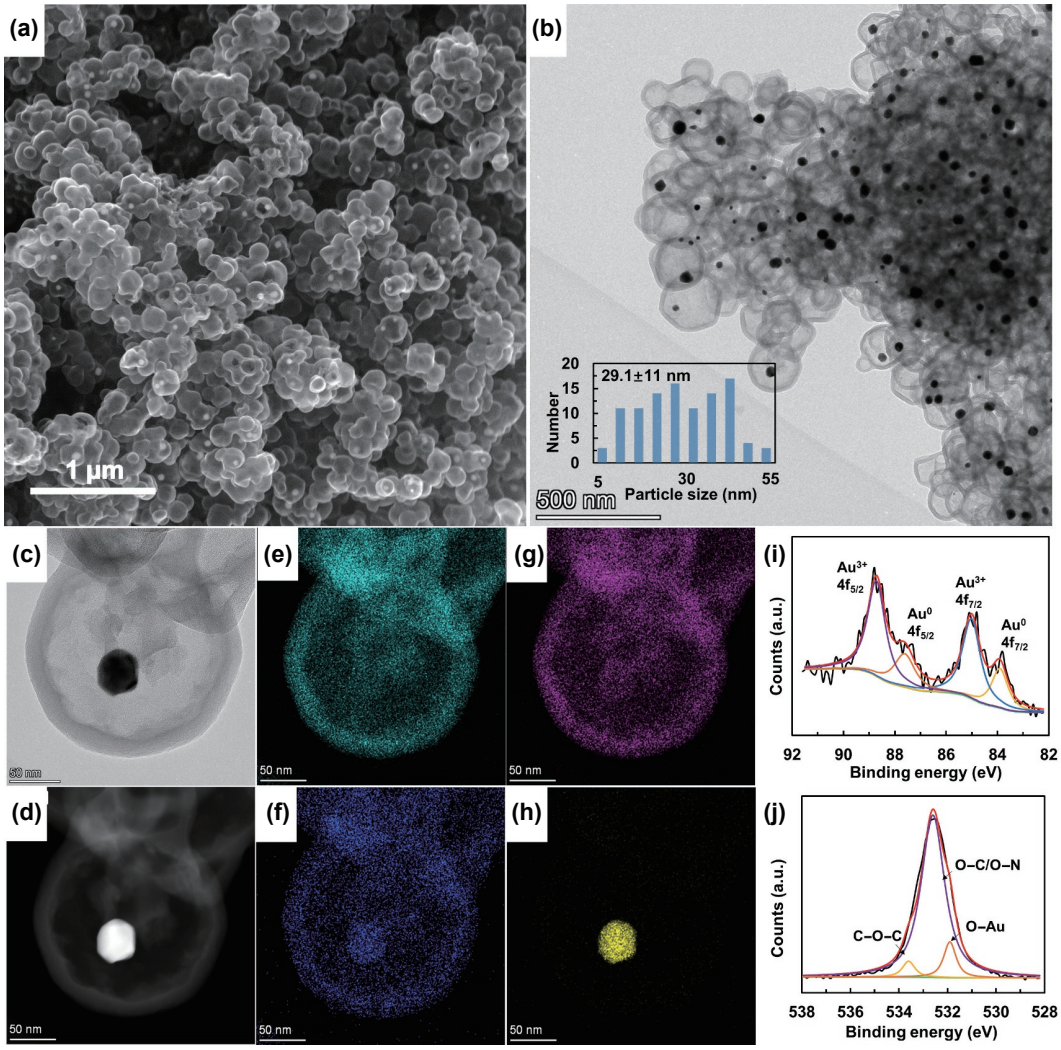

Figure 4 (a) SEM image, ((b) and (c)) TEM images, (d) HAADF image, and elemental mapping images of (e) C, (f) O, (g) N, (h) Au, and XPS deconvolution spectra of (i) Au 4f and (j) O 1s of Au@HPC-F_2.

would turn into metallic and oxide forms during the carbonization process, and the produced sub-nanoparticles would merge into nanoparticles [33, 34], resulting in the formation of Au@HPC-F_2 core–shell structure.

The high specific surface area and the existence of micro and mesopores in the carbon shell of Au@HPC-F_2 could enhance mass transfer and diffusion, which would benefit its catalytic performance. On the other hand, the carbon cage could prevent the aggregation of Au nanoparticles, thus avoiding the loss of their catalytic performance [35, 36]. Therefore, we finally investigated the behavior of Au@HPC-F_2 as a heterogeneous catalyst for the reduction of nitrobenzene (NB) in water. In general, 0.066 mg of catalyst was dispersed in a 6.6 mL of 0.11 mM NB aqueous solution and its catalytic kinetic was monitored with ultraviolet–visible (UV–vis) adsorption spectroscopy. Firstly, HPC-F_2 was tested to exclude the effect of the carbon shell. As shown in Fig. 5(a), small changes in NB concentration could be observed and no sign of aniline formation appeared, indicating HPC-F_2 contributed little in the NB reduction reaction. Next, Au@HPC-F_2 was characterized. As shown in Fig. 5(b), a rapid conversion of NB (~ 270 nm) to aniline (~ 230 nm) could be observed despite the relatively small amount of Au@HPC-F_2. Within 2 min, the intensity of NB decreased dramatically and the aniline signal increased accordingly. After 5 min, the conversion of NB to aniline was almost finished [37]. Moreover, increasing the amount of Au@HPC-F_2 could further accelerate the conversion rate (Fig. 5(c)). The performance is comparable to or even better than several supported AuNPs catalysts in literatures (Table S2 in the ESM). Finally, a home-made reactor packed with Au@HPC-F_2 was designed to study the long-term stability of the catalyst. As

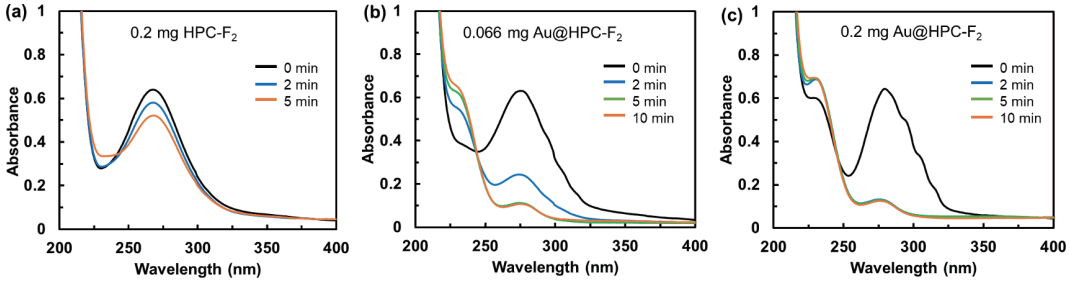

Figure 5 UV–vis spectra during the NB reduction in the presence of HPC-F_2 and Au@HPC-F_2 catalysts.

shown in Fig. S9 in the ESM, the reaction lasted for more than 24 h and Au@HPC-F_2 still remained high catalytic activity. Additionally, the morphology of the catalyst after stability test was well preserved (Fig. S10 in the ESM). These results indicated the high efficiency and high stability of the obtained Au@HPC-F_2.

In conclusion, we have developed a facile and adaptable synthesis protocol of HPCs through a two-step heating process using ZIF-8 and TFTPN. TFTPN reacted with 2-MeI of ZIF-8 to afford polymer-coated ZIF-8 nanocomposites in the first heating step, followed by extensive reaction between TFTPN and 2-MeI in the second step, leading to further coordination dislocation and structure collapse. The obtained HPCs were heteroatom doped, showed large specific surface area of up to ~ 580 $m^2 \cdot g^{-1}$, and consisted of micro and mesoporous structure. In addition, the synthesis protocol was used for the preparation of Au@HPCs yolk–shell nanocatalyst, which exhibited good catalytic activity in nitrobenzene reduction. We expect this strategy to be extended in the design and synthesis of novel HPCs and their composites.

Acknowledgements

We thank the financial support from the Shenzhen Science and Technology Program (No. KQTD20170810141424366), the 2019 Special Program for Central Government Guiding Local Science and Technology Development: Environmental Purification Functional Materials Research Platform, the Program for Guangdong Introducing Innovative and Entrepreneurial Teams (No. 2017ZT07C291), the National Natural Science Foundation of China (Nos. 22005260 and 22078276), the Guangdong Basic and Applied Basic Research Foundation (No. 2019A1515110185), and the Shenzhen Key Laboratory of Advanced Materials Product Engineering (No. ZDSYS20190911164401990).

Electronic Supplementary Material: Supplementary material (experimental details, thermal analysis, SEM imaging, characterizations for ZIF-8/F, and ZIF-8/$AuCl_4^-$ composite) is available in the online version of this article at https://doi.org/10.1007/s12274-022-4201-1.

References

[1] Ren, J. C.; Huang, Y. L.; Zhu, H.; Zhang, B. H.; Zhu, H. K.; Shen, S. H.; Tan, G. Q.; Wu, F.; He, H.; Lan, S. et al. Recent progress on MOF-derived carbon materials for energy storage. *Carbon Energy* **2020**, *2*, 176–202.

[2] Zhang, R. P.; Li, W. C.; Hao, G. P.; Lu, A. H. Confined nanospace pyrolysis: A versatile strategy to create hollow structured porous carbons. *Nano Res.* **2021**, *14*, 3159–3173.

[3] Fan, H. L.; Hu, X.; Zhang, S.; Xu, Z. X.; Gao, G. M.; Zheng, Y.; Hu, G. Z.; Chen, Q. F.; AlGarni, T. S.; Luque, R. Flower-like carbon cathode prepared via *in situ* assembly for Zn-ion hybrid supercapacitors. *Carbon* **2021**, *180*, 254–264.

[4] Hou, C. C.; Wang, Y.; Zou, L. L.; Wang, M.; Liu, H. W.; Liu, Z.; Wang, H. F.; Li, C. X.; Xu, Q. A gas-steamed MOF route to P-doped open carbon cages with enhanced Zn-ion energy storage capability and ultrastability. *Adv. Mater.* **2021**, *33*, 2101698.

[5] Lu, X. F.; Fang, Y. J.; Luan, D. Y.; David Lou, X. W. Metal-organic frameworks derived functional materials for electrochemical energy storage and conversion: A mini review. *Nano Lett.* **2021**, *21*, 1555–1565.

[6] Ni, W.; Xue, Y. F.; Zang, X. G.; Li, C. X.; Wang, H. Z.; Yang, Z. Y.; Yan, Y. M. Fluorine doped cagelike carbon electrocatalyst: An insight into the structure-enhanced CO selectivity for CO_2 reduction at high overpotential. *ACS Nano* **2020**, *14*, 2014–2023.

[7] Liu, Y.; Li, Q. Y.; Guo, X.; Kong, X. D.; Ke, J. W.; Chi, M. F.; Li, Q. X.; Geng, Z. G.; Zeng, J. A highly efficient metal-free electrocatalyst of F-doped porous carbon toward N_2 electroreduction. *Adv. Mater.* **2020**, *32*, 1907690.

[8] Zhai, Y.; Wang, F. M.; Zhang, X. B.; Lv, G. J.; Wu, Y. Z.; Jiang, T.; Zhang, Q.; Li, M. Y.; Li, M. Y.; Liu, Y. K. Directional design and synthesis of high-yield hollow Fe-MFI zeolite encapsulating ultra-small Fe_2O_3 nanoparticles by using mother liquid. *Nano Res.* **2021**, *14*, 4304–4313.

[9] Chen, C. J.; Song, J. W.; Zhu, S. Z.; Li, Y. J.; Kuang, Y. D.; Wan, J. Y.; Kirsch, D.; Xu, L. S.; Wang, Y. B.; Gao, T. T. et al. Scalable and sustainable approach toward highly compressible, anisotropic, lamellar carbon sponge. *Chem* **2018**, *4*, 544–554.

[10] Zhang, F.; Feng, Y. Y.; Feng, W. Three-dimensional interconnected networks for thermally conductive polymer composites: Design, preparation, properties, and mechanisms. *Mater. Sci. Eng. :R:Rep.* **2020**, *142*, 100580.

[11] Gadipelli, S.; Guo, Z. X. Tuning of ZIF-derived carbon with high activity, nitrogen functionality, and yield—A case for superior CO_2 capture. *ChemSusChem* **2015**, *8*, 2123–2132.

[12] Ma, X. C.; Chen, R. F.; Zhou, K.; Wu, Q. D.; Li, H. L.; Zeng, Z.; Li, L. Q. Activated porous carbon with an ultrahigh surface area derived from waste biomass for acetone adsorption, CO_2 capture, and light hydrocarbon separation. *ACS Sustainable Chem. Eng.* **2020**, *8*, 11721–11728.

[13] Wei, R. P.; Dong, Y. T.; Zhang, Y. Y.; Kang, X. Y.; Sheng, X.; Zhang, J. M. Hollow cubic MnS-CoS_2-NC@NC designed by two kinds of nitrogen-doped carbon strategy for sodium ion batteries with ultraordinary rate and cycling performance. *Nano Res*., in press, https://doi.org/10.1007/s12274-021-3973-z.

[14] Gao, H.; Sun, L. M.; Li, M. G.; Zhan, W. W.; Wang, X. J.; Han, X. G. Fabricating a hollow cuboctahedral structure for N-doped carbon coated p-n heterojunctions towards high-performance photocatalytic organic transformation. *Nano Res*., in press, DOI: 10.1007/s12274-021-4016-5.

[15] Yang, Q. H.; Yang, C. C.; Lin, C. H.; Jiang, H. L. Metal-organic-framework-derived hollow N-doped porous carbon with ultrahigh concentrations of single Zn atoms for efficient carbon dioxide conversion. *Angew. Chem., Int. Ed.* **2019**, *58*, 3511–3515.

[16] Tan, Y. C.; Zeng, H. C. Self-templating synthesis of hollow spheres of MOFs and their derived nanostructures. *Chem. Commun.* **2016**, *52*, 11591–11594.

[17] Zhang, W.; Jiang, X. F.; Zhao, Y. Y.; Carné-Sánchez, A.; Malgras, V.; Kim, J.; Kim, J. H.; Wang, S. B.; Liu, J.; Jiang, J. S. et al. Hollow carbon nanobubbles: Monocrystalline MOF nanobubbles and their pyrolysis. *Chem. Sci.* **2017**, *8*, 3538–3546.

[18] Xia, B. Y.; Yan, Y.; Li, N.; Wu, H. B.; Lou, X. W.; Wang, X. A metal-organic framework-derived bifunctional oxygen electrocatalyst. *Nat. Energy* **2016**, *1*, 15006.

[19] Meng, J. S.; Niu, C. J.; Xu, L. H.; Li, J. T.; Liu, X.; Wang, X. P.; Wu, Y. Z.; Xu, X. M.; Chen, W. Y.; Li, Q. et al. General oriented formation of carbon nanotubes from metal-organic frameworks. *J. Am. Chem. Soc.* **2017**, *139*, 8212–8221.

[20] Huang, L. Q.; Luo, Z. Y.; Luo, M. W.; Zhang, Q.; Zhu, H.; Shi, K. Y.; Zhu, S. P. One-step synthesis of nitrogen-fluorine dual-doped porous carbon for supercapacitors. *J. Energy Storage* **2021**, *38*, 102509.

[21] Huang, L. Q.; Xiang, Y.; Luo, M. W.; Zhang, Q.; Zhu, H.; Shi, K. Y.; Zhu, S. P. Hierarchically porous carbon with heteroatom doping for the application of Zn-ion capacitors. *Carbon* **2021**, *185*, 1–8.

[22] Kim, M. J.; Xu, X. T.; Xin, R. J.; Earnshaw, J.; Ashok, A.; Kim, J.; Park, T.; Nanjundan, A. K.; El-Said, W. A.; Yi, J. W. et al. KOH-activated hollow ZIF-8 derived porous carbon: Nanoarchitectured control for upgraded capacitive deionization and supercapacitor. *ACS Appl. Mater. Interfaces* **2021**, *13*, 52034–52043.

[23] Son, I. S.; Oh, Y.; Yi, S. H.; Im, W. B.; Chun, S. E. Facile fabrication of mesoporous carbon from mixed polymer precursor of PVDF and PTFE for high-power supercapacitors. *Carbon* **2020**, *159*, 283–291.

[24] de Silva, A. J.; Contreras, M. M.; Nascimento, C. R.; da Costa, M. F. Kinetics of thermal degradation and lifetime study of poly(vinylidene fluoride) (PVDF) subjected to bioethanol fuel accelerated aging. *Heliyon* **2020**, *6*, e04573.

[25] Shabani-Nooshabadi, M.; Karimian-Taheri, F. Electrosynthesis of a polyaniline/zeolite nanocomposite coating on copper in a three-step process and the effect of current density on its corrosion protection performance. *RSC Adv.* **2015**, *5*, 96601–96610.

[26] Bhattacharyya, S.; Pang, S. H.; Dutzer, M. R.; Lively, R. P.; Walton, K. S.; Sholl, D. S.; Nair, S. Interactions of SO_2-containing acid gases with ZIF-8: Structural changes and mechanistic investigations. *J. Phys. Chem. C* **2016**, *120*, 27221–27229.

[27] Zhang, B.; Wei, M. F.; Mao, H. Y.; Pei, X. K.; Alshmimri, S. A.; Reimer, J. A.; Yaghi, O. M. Crystalline dioxin-linked covalent organic frameworks from irreversible reactions. *J. Am. Chem. Soc.* **2018**, *140*, 12715–12719.

[28] Li, F. Y.; Xiao, Y. C.; Chung, T. S.; Kawi, S. High-performance thermally self-cross-linked polymer of intrinsic microporosity (PIM-1) membranes for energy development. *Macromolecules* **2012**, *45*, 1427–1437.

[29] Clark, D. T.; Kilcast, D.; Adams, D. B.; Musgrave, W. K. R. An ESCA study of the molecular core binding energies of the fluorobenzenes. *J. Electron Spectros. Relat. Phenom.* **1972–1973**, *1*, 227–250.

[30] Ebrahimpour, Z.; Mansour, N. Annealing effects on electrical behavior of gold nanoparticle film: Conversion of ohmic to non-ohmic conductivity. *Appl. Surf. Sci.* **2017**, *394*, 240–247.

[31] Deng, X. Y.; Li, J. J.; Shan, Z.; Sha, J. W.; Ma, L. Y.; Zhao, N. Q. A N, O co-doped hierarchical carbon cathode for high-performance Zn-ion hybrid supercapacitors with enhanced pseudocapacitance. *J. Mater. Chem. A* **2020**, *8*, 11617–11625.

[32] Zeng, L.; Dai, C. H.; Liu, B.; Xue, C. Oxygen-assisted stabilization of single-atom Au during photocatalytic hydrogen evolution. *J. Mater. Chem. A* **2019**, *7*, 24217–24221.

[33] Yang, T. Y.; Ling, H. J.; Lamonier, J. F.; Jaroniec, M.; Huang, J.; Monteiro, M. J.; Liu, J. A synthetic strategy for carbon nanospheres impregnated with highly monodispersed metal nanoparticles. *NPG Asia Mater.* **2016**, *8*, e240.

[34] Couchman, P. R.; Jesser, W. A. Thermodynamic theory of size dependence of melting temperature in metals. *Nature* **1977**, *269*, 481–483.

[35] Zhou, J. J.; Duan, B.; Fang, Z.; Song, J. B.; Wang, C. X.; Messersmith, P. B.; Duan, H. W. Interfacial assembly of mussel-inspired Au@Ag@ polydopamine core–shell nanoparticles for recyclable nanocatalysts. *Adv. Mater.* **2014**, *26*, 701–705.

[36] Mitsudome, T.; Yamamoto, M.; Maeno, Z.; Mizugaki, T.; Jitsukawa, K.; Kaneda, K. One-step synthesis of core-gold/shell-ceria nanomaterial and its catalysis for highly selective semihydrogenation of alkynes. *J. Am. Chem. Soc.* **2015**, *137*, 13452–13455.

[37] Choi, S.; Lee, H. J.; Oh, M. Facile synthesis of Au or Ag nanoparticles-embedded hollow carbon microspheres from metal-organic framework hybrids and their efficient catalytic activities. *Small* **2016**, *12*, 2425–2431.